



HAL
open science

Laboratory evaluation of the (VIS, IR) scattering matrix of complex-shaped ragweed pollen particles

Danaël Cholleton, Emilie Bialic, Antoine Dumas, Pascal Kaluzny, Patrick Rairoux, Alain Miffre

► **To cite this version:**

Danaël Cholleton, Emilie Bialic, Antoine Dumas, Pascal Kaluzny, Patrick Rairoux, et al.. Laboratory evaluation of the (VIS, IR) scattering matrix of complex-shaped ragweed pollen particles. *Journal of Quantitative Spectroscopy and Radiative Transfer*, 2020, 254, pp.107223. 10.1016/j.jqsrt.2020.107223 . hal-02967601

HAL Id: hal-02967601

<https://hal.science/hal-02967601>

Submitted on 22 Aug 2022

HAL is a multi-disciplinary open access archive for the deposit and dissemination of scientific research documents, whether they are published or not. The documents may come from teaching and research institutions in France or abroad, or from public or private research centers.

L'archive ouverte pluridisciplinaire **HAL**, est destinée au dépôt et à la diffusion de documents scientifiques de niveau recherche, publiés ou non, émanant des établissements d'enseignement et de recherche français ou étrangers, des laboratoires publics ou privés.



Distributed under a Creative Commons Attribution - NonCommercial 4.0 International License

Laboratory evaluation of the (VIS, IR) scattering matrix of complex-shaped ragweed pollen particles

Danaël Cholleton^{1,2}, Emilie Bialic², Antoine Dumas², Pascal Kaluzny², Patrick Rairoux¹ and Alain Miffre¹

¹University of Lyon, Université Claude Bernard Lyon 1,

CNRS, Institut Lumière Matière, F-69622, Villeurbanne, France

²TERA Sensor, ZI Rousset, 296 Avenue Georges Vacher, 13790, Rousset, France

Corresponding author: A. Miffre (alain.miffre@univ-lyon1.fr)

Abstract

Ragweed or *Ambrosia artemisiifolia* pollen is an important atmospheric constituent affecting the Earth's climate and public health. The literature on light scattering by pollens embedded in ambient air is however rather sparse: polarization measurements are limited to the sole depolarization ratio and pollens are beyond the reach of numerically exact light scattering models mainly due to their tens of micrometre size. Also, ragweed pollen presents a very complex shape, with a small-scale external structure exhibiting spikes that bears some resemblance with coronavirus, but also apertures and micrometre holes. In this paper, to face such a complexity, a controlled-laboratory experiment is proposed to evaluate the scattering matrix of ragweed pollen embedded in ambient air. It is based on a newly-built polarimeter, operating in the infra-red spectral range, to account for the large size of ragweed pollen. Moreover, the ragweed scattering matrix is also evaluated in the visible spectral range to reveal the spectral dependence of the ragweed scattering matrix within experimental error bars. As an output, precise spectral and polarimetric fingerprints for large size and complex-shaped ragweed pollen particles are then provided. We believe our laboratory experiment may interest the light scattering community by complementing other light scattering experiments and proposing outlooks for numerical work on large and complex-shaped particles.

Keywords

Scattering, ragweed pollen, scattering matrix, polarimetry, spectroscopy.

1. Introduction

Pollens are important atmospheric constituents with multitude of impacts. Through allergenic diseases, pollen exposure leads to pollinosis [1], clinically characterized by bronchial asthma or rhinoconjunctivitis with annual periodicity. Ragweed pollen or *Ambrosia artemisiifolia* represents one of the major seasonal allergens in Europe and Northern America [2–4] and induces asthma about twice as often as other pollens [5]. To figure out, 15.8 million persons in Europe are clinically ragweed sensitised, for an economic cost in Europe of about 7 billion euros [6]. This pollen allergenicity is further enhanced by atmospheric pollution by particulate matter [7], which modifies the pollen morphological structure [8]. Pollens also contribute to the Earth's climate through light scattering and extinction and by acting as cloud condensation and ice nuclei [9], hence influencing regional precipitations [10,11]. At a local scale, the infra-red downwelling flux can be increased by up to eight times the monthly mean at high pollen concentrations [12]. Hence, climate warming promotes the spread of ragweed in central Europe [13] and ragweed production and growth is directly impacted by rising atmospheric carbon dioxide concentrations [14]. Due to climate change, the ragweed pollen season starts earlier and has an increased duration [15]. Moreover, each ragweed plant produces millions of pollen grains that can be transported over large distances and be observed far from source regions [5], up to a continental scale [16]. Hence, atmospheric transport models have been developed to forecast pollen concentrations [17] by considering meteorological data, emission maps and pollen counts [18].

With about twenty micrometres volume equivalent diameter, ragweed pollen grains are rather large particles [19]. The ragweed shape is overall spherical but exhibits a smaller scale complex external structure with spikes, apertures and sub-micrometer holes, as well as an heterogeneous cell content [20]. As recently underscored by Liu et al. [21], accounting for this complex geometry is key for radiative transfer applications involving pollens. To study the size and the morphology of ragweed, the most widely-used methodology is the historical approach, based on optical and scanning electron microscopy after gravitational deposition on a substrate [22]. Deep learning recently considerably improved this methodology [23]. In the last two decades, complementary optical methodologies have been developed, based on laser-induced fluorescence, interferometry, or / and light scattering. In laser-induced fluorescence, the pollens lifetime and emission spectra are recorded from the UV to the NIR spectral range to allow identifying

fingerprints [24–26]. Pollens holography allows image-based recognition [27,28]. Moreover, as published by M. Berg and G. Videen [29], a cluster of ragweed pollen particles can be imaged in-situ using digital in-line holography to discern the ragweed single-particle size and shape. The sensitivity of light scattering to the pollens size and shape has been studied for several decades when pollen grains are embedded in aqueous solutions [30–32]. More recently, light scattering by pollens has been studied when pollens are in a fixed orientation as deposited on a holder in [33–35] or more recently in [36]. Concerning airborne pollens, forward and side scattering have been compared in [37] and the spectral dependence of forward light scattering patterns has been studied in [38], without however considering the light polarization property, which may vary during the scattering process for non-spherical particles [39], as for ragweed pollen particles. The light depolarization ratio of several pollens has been evaluated in the atmosphere in [40–43]. However, such polarization measurements remain sparse and the measured atmospheric depolarization ratio may differ [44,45] from that specific to ragweed since pollens are usually present in the atmosphere in the form of particle mixtures. Furthermore, these polarization measurements are limited to the sole particles depolarization ratio, while the ragweed ability to scatter light should be specified for each polarization state by providing its scattering matrix. Likewise, due to their large size, and the small-scale morphological structures of ragweed pollen grains are beyond the reach of numerically exact light-scattering models [46,47]. Historically, the Lorenz-Mie theory has been applied to study the influence of the membrane thickness and the pollen refractive index on the scattered light intensity using a core/shell model [48]. However, as well-known [49], the spherical model cannot reproduce the polarization properties of ragweed complex-shaped grains. Interestingly, the ragweed overall spherical shape with regular spikes bears some resemblance with that of coronavirus, which has been recently studied using T-Matrix numerical code by D. Petrov [50]. However, applying this numerical code to ragweed pollen particles a priori remains challenging due to their larger size. Also, surface roughness should be considered for such large particles. In this context, controlled laboratory measurements of the ragweed pollen scattering matrix may help to discuss the underlying assumptions inherent to such light scattering numerical models for pollens.

On account of the above literature, the scattering matrix of ragweed pollen particles should be evaluated by taking into account their large size and their complex shape, which is key for radiative transfer applications [21]. The novelty of our contribution is then twofold. Firstly, a controlled-laboratory experiment has been developed to precisely evaluate the scattering matrix of ragweed pollen particles embedded in ambient air. It is based on a newly-built laboratory polarimeter, operating in the infra-red spectral range to account for the large size of ragweed pollen particles. As a second novelty, this ragweed scattering matrix is evaluated also in the visible spectral range at 532 nm wavelength, to reveal precise spectral and polarimetric fingerprints for ragweed. The paper is organised as follows. Section 2 details our laboratory methodology to precisely evaluate the ragweed scattering matrix at two wavelengths with corresponding sources of uncertainties. Section 3 is dedicated to the characterization of the size and the shape of our ragweed samples, based on scanning electron microscopy images and evaluation of their size distribution. The evaluation of the ragweed scattering matrix at two wavelengths is presented in Section 4. The paper ends with a conclusion and proposes outlooks.

2. Light scattering by ragweed pollen

2.1. Scattering matrix formalism

We here consider elastic scattering of an electromagnetic radiation (wavelength λ , polarization state π) by an ensemble of ragweed pollen particles embedded in ambient air. While the wavelength is preserved during the elastic scattering process, the polarization states of the incident and scattered radiations (respective wave-vectors $\mathbf{k}_0(\lambda)$ and $\mathbf{k}(\lambda)$) may differ and be analysed in the framework of the scattering matrix formalism [39]. In this formalism, the polarization states of the incident and scattered radiations are described by the incident and scattered Stokes vectors $(\mathbf{S}_0) = [I_0, Q_0, U_0, V_0]^t$ and $(\mathbf{S}) = [I, Q, U, V]^t$, where I corresponds to the light intensity, Q and U are parameters describing the linear polarization state, while V refers to circular polarization. The wave-vectors $(\mathbf{k}_0, \mathbf{k})$ define the scattering angle, used as a reference plane for the Stokes vectors. By assuming ragweed pollen particles to be randomly oriented and to have their mirror particles in equal number in the particles ensemble, the incident and scattered Stokes vectors relate as:

$$\begin{pmatrix} I \\ Q \\ U \\ V \end{pmatrix} = \frac{\lambda^2}{4\pi^2 d^2} \begin{bmatrix} F_{11}(\lambda) & F_{12}(\lambda) & 0 & 0 \\ F_{12}(\lambda) & F_{22}(\lambda) & 0 & 0 \\ 0 & 0 & F_{33}(\lambda) & F_{34}(\lambda) \\ 0 & 0 & -F_{34}(\lambda) & F_{44}(\lambda) \end{bmatrix} \begin{pmatrix} I_0 \\ Q_0 \\ U_0 \\ V_0 \end{pmatrix} \quad (1)$$

where d is the distance from the ragweed pollen particles to the light detector. In Eq. (1), the dimensionless scattering matrix elements $F_{ij}(\lambda)$ (i, j from 1 to 4) depend on the wavelength of the radiation, the scattering angle, the size, the shape and the refractive index of the ragweed pollen particles. If ragweed pollen particles were spherical, the scattering matrix elements would simplify [51] since for homogeneous spherical particles, $F_{11}(\lambda) = F_{22}(\lambda)$ and $F_{33}(\lambda) = F_{44}(\lambda)$. The scattering matrix elements can be normalized with respect to the scattering phase function $F_{11}(\lambda)$:

$$f_{ij}(\lambda) = F_{ij}(\lambda)/F_{11}(\lambda) \quad (2)$$

which at most equal unity, as detailed in light scattering textbooks [52].

2.2. Laboratory (VIS, IR) light scattering experimental setup for ragweed

Fig. 1 schemes our laboratory light scattering experimental set-up, based on two laboratory polarimeters operating at wavelength $\lambda_{VIS} = 532$ nm and $\lambda_{IR} = 1064$ nm respectively, to account for the spectral dependence of the ragweed pollen scattering matrix. Ragweed pollen particles are embedded in laboratory ambient air as described in Section 3.1. While the λ_{VIS} -polarimeter is similar to our previous work [53], the λ_{IR} -polarimeter is new and has been specifically designed to evaluate light scattering by ragweed pollen grains, which exhibit a size in the tens of micrometres range. Special care has been taken to precisely define the Stokes vector of the incident radiation at each wavelength. The polarization state of the scattered radiation is analysed with a quarter-wave plate (QWP) and a retro-reflecting polarizing beam-splitter cube (PBC). At wavelength λ_{IR} , the intensity of the s -polarization component of the scattered radiation is measured with an Si avalanche photodiode cooled at 0°C . To minimize wavelength cross-talks, a selective interference filter is inserted before the photodiode. After minimizing the polarization and wavelength cross-talks (see Section 2.4), to add precision in the evaluation of the scattering matrix elements, the scattered light intensity is measured for a complete rotation of the QWP. The radiation scattered by ragweed pollens grains is discriminated from light scattering by laboratory ambient air by achieving time-resolved measurements synchronized with the laser pulse, hence addressing the time-of-flight $2d/c$ taken by a laser pulse to reach the detector after light scattering. The scattered intensity by ragweed pollens grains is then evaluated by subtracting the intensity scattered by laboratory ambient air from the total intensity scattered by ragweed and ambient air. As underscored in Fig. 1, both polarimeters evaluate the scattering matrix elements of the same ragweed sample and operate at a scattering angle of 178° , close to 180° , which can be interesting for remote sensing applications. The scattering angle slightly differs from strict backscattering to allow the Eq. (1) scattering matrix elements to be a priori independent from $F_{22}(\lambda)$. Indeed, at strict backscattering, only $F_{11}(\lambda)$ and $F_{22}(\lambda)$ would appear in Eq. (1) since $F_{33}(\lambda) = -F_{22}(\lambda)$, $F_{44}(\lambda) = F_{11}(\lambda) - 2F_{22}(\lambda)$, while $F_{12}(\lambda) = F_{34}(\lambda) = 0$.

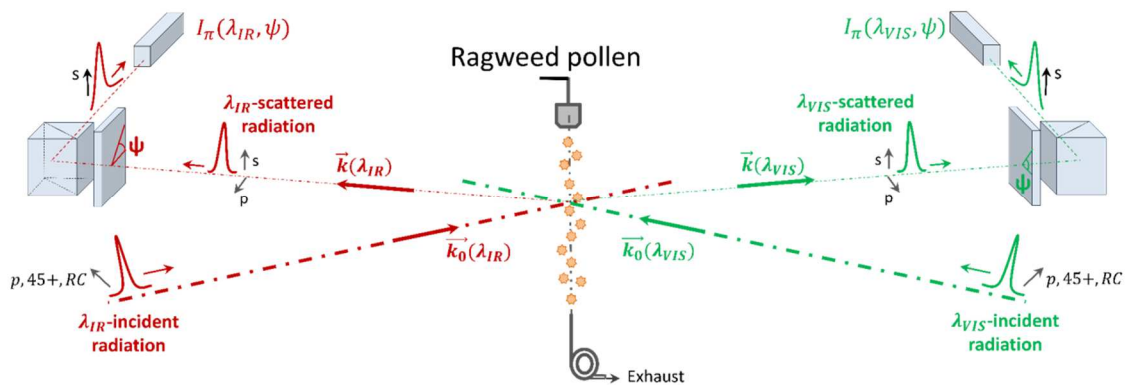


Fig. 1. Scheme of our laboratory experimental set-up for ragweed scattering matrix evaluation at two wavelengths ($\lambda_{VIS} = 532$ nm and $\lambda_{IR} = 1064$ nm). The 178° scattering angle has been exaggerated to ease the reading. Ragweed pollens grains are embedded in laboratory ambient air as described in Section 3.1.

2.3. Methodology for evaluating the ragweed scattering matrix elements

The light intensity scattered by ragweed pollen grains is evaluated by accounting for the successive Mueller matrices encountered in Fig. 1 by the $(\lambda_{VIS}, \lambda_{IR})$ laser pulses. If $P_0(\lambda)$ is the incident laser power at wavelength λ and the polarization state of the incident radiation is defined with a polarizer $[\mathbf{P}]$, the detected scattered intensity at wavelength λ is given by:

$$I_\pi(\lambda) = \frac{\eta(\lambda)P_0(\lambda)}{d^2} (\mathbf{P}_j)[\mathbf{PBC}][\mathbf{QWP}][\mathbf{F}(\lambda)][\mathbf{P}](\mathbf{S}_0) \quad (3)$$

Where $\eta(\lambda)$ is the electro-optics efficiency of the light detector and $(\mathbf{P}_j) = [1, 0, 0, 0]$ is a unitary projector as the light detector is solely sensitive to the first component of the scattered Stokes vector, i.e. the light intensity. $[\mathbf{QWP}]$ and $[\mathbf{PBC}]$ are the Mueller matrices of the quarter-wave plate and the reflecting PBC respectively. The π -subscript is used in Eq. (3) to refer to the polarization state of the incident radiation defined by the Stokes vector $[\mathbf{P}](\mathbf{S}_0)$. To evaluate the five normalized ragweed scattering matrix elements $f_{ij}(\lambda) = F_{ij}(\lambda)/F_{11}(\lambda)$, three successive incident polarization states are required, for example $\pi = (p, 45+, RC)$, corresponding to the following Stokes vectors $[\mathbf{P}](\mathbf{S}_0) = [1, 1, 0, 0], [1, 0, 1, 0]$ and $[1, 0, 0, 1]$ respectively. If ψ represents the angle between the QWP-fast axis and the scattering plane, using [54] for $[\mathbf{QWP}]$ and $[\mathbf{PBC}]$, the detected scattered intensity $I_\pi(\lambda, \psi)$ for incident polarization state π is given by:

$$I_\pi(\lambda, \psi) = I_{11}(\lambda) \times [a_\pi(\lambda) - b_\pi(\lambda) \sin(2\psi) - c_\pi(\lambda) \cos(4\psi) - d_\pi(\lambda) \sin(4\psi)] \quad (4)$$

Where $I_{11}(\lambda) = \eta(\lambda)P_0(\lambda)F_{11}(\lambda)/4d^2$ and ψ is counted counter-clockwise for an observer looking from the PBC to the ragweed pollen particles. Interestingly, the $a_\pi(\lambda), b_\pi(\lambda), c_\pi(\lambda), d_\pi(\lambda)$ coefficients are combinations of the normalized scattering matrix elements $f_{ij}(\lambda)$ and depend on the polarization state of the incident radiation, as referred to by the π -subscript. After a few calculations detailed in Miffre et al. [53], the normalized scattering matrix elements then express as:

$$f_{12}(\lambda) = 2c_{RC}/(a_{RC} + c_{RC}) \quad (5a)$$

$$f_{34}(\lambda) = 2d_{RC}/(a_{RC} + c_{RC}) \quad (5b)$$

$$f_{44}(\lambda) = -b_{RC}/(a_{RC} + c_{RC}) \quad (5c)$$

$$f_{33}(\lambda) = 2d_{45+}/(a_{45+} + c_{45+}) \quad (5d)$$

$$f_{22}(\lambda) = [f_{12}(\lambda) \times (c_p - a_p) + 2c_p]/(a_p + c_p) \quad (5e)$$

Where, to ease the reading, the dependence of $a_\pi(\lambda), b_\pi(\lambda), c_\pi(\lambda), d_\pi(\lambda)$ with wavelength λ has been omitted. Hence, the normalized scattering elements $f_{33}(\lambda)$ and $f_{44}(\lambda)$ can be retrieved using incident polarization states (45+) and (RC) respectively, while the normalized scattering matrix elements $f_{12}(\lambda)$ and $f_{34}(\lambda)$ can be retrieved either from (45+) or (RC) incident polarization state. From the evaluation of $f_{12}(\lambda)$, incident polarization state (p) allows retrieving $f_{22}(\lambda)$. By adjusting the detected scattered intensity with Eq. (4) over a complete rotation of the QWP, the coefficients $a_\pi(\lambda)$ to $d_\pi(\lambda)$ can be precisely determined, allowing precise evaluations of the normalized scattering matrix elements by applying Eqs. (5). Fig. 2 shows the variations of $I_\pi(\lambda, \psi)/I_{11}(\lambda)$ for given scattering matrix elements at incident polarization states $\pi = (p, 45+, RC)$ when varying the modulation angle ψ . Following Eqs. (4, 5), the minima in Fig. 2(a), which are equal to $2(1 - f_{22})$, are null for spherical particles and the (p)- polarization curve is $\pi/2$ -periodic as coefficients $b_p(\lambda)$ and $d_p(\lambda)$ are zero. In Fig. 2(b) corresponding to 45+-incident polarization state, the detected scattered intensity $I_{45+}(\lambda)/I_{11}(\lambda)$ is π -periodic as $b_{45+}(\lambda)$ is not null. The difference between two successive maxima or minima in Fig. 2(b) is proportional to $f_{34}(\lambda)$. In Fig. 2(c) corresponding to RC-incident polarization state, the detected scattered intensity $I_{RC}(\lambda, \psi)/I_{11}(\lambda)$ is also π -periodic, with minima equal to $2(1 - f_{44}(\lambda))$.

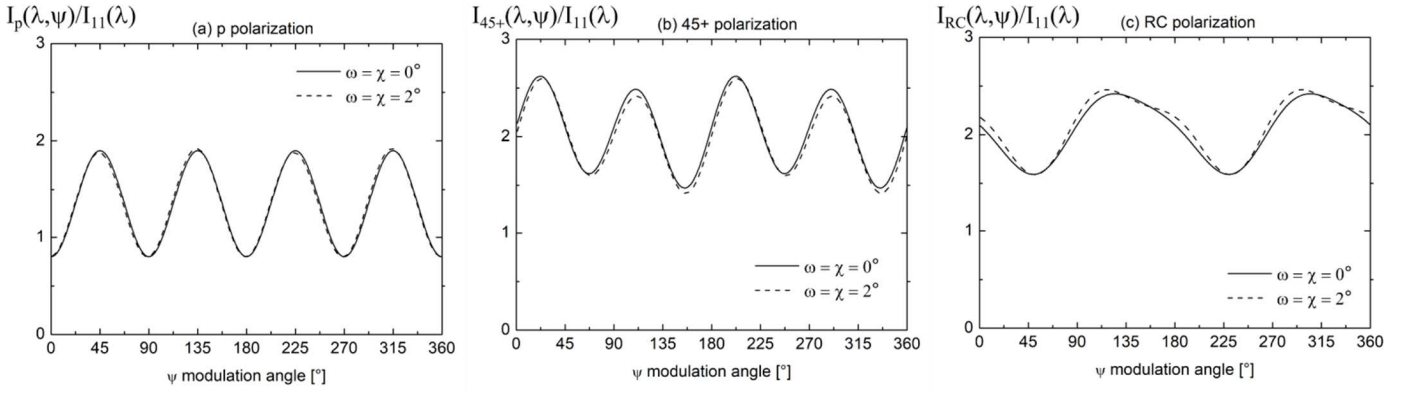


Fig. 2. Numerical simulation of the detected scattered light intensity $I_{\pi}(\lambda, \psi)/I_{11}(\lambda)$ as a function of the ψ modulation angle of the QWP following Eq. (4), for $f_{22}(\lambda) = 0.6$, $f_{33}(\lambda) = -0.5$, $f_{44}(\lambda) = -0.2$, $f_{12}(\lambda) = -0.05$ and $f_{34}(\lambda) = -0.05$, at incident polarization states $\pi = (p, 45+, RC)$ from panels (a) to (c). As detailed in Section 2.4, dashed curves show the modification induced in $I(\lambda, \psi)/I_{11}(\lambda)$ when considering a 2° deviation in both $\omega(\lambda)$ and $\chi(\lambda)$ for the incident polarization state.

2.4. Accuracy on ragweed scattering matrix elements $f_{ij}(\lambda)$

Special care has been taken to precisely evaluate the uncertainties on the retrieved scattering matrix elements $f_{ij}(\lambda)$ at wavelength λ .

- Statistical errors on $f_{ij}(\lambda)$ may arise from fluctuations in the probed scattering volume of the ragweed pollen particles number concentration. If the ragweed pollen number concentration is stable over a complete rotation of the QWP (see Section 4.2), fluctuations over a one second timescale may occur and add noise to the detected scattered intensity. As explained in [53], we overcame this difficulty by normalizing the detected scattered light intensity with a polarization insensitive photodetector.
- *Systematic errors* may occur if the incident polarization states differ from strict $(p, 45+, RC)$ polarization states, or / and, through possible mismatch between the s -polarization axis of the emitted and detected scattered radiations, that may lead to undesirable polarization cross-talks. Also, wavelength cross-talks may occur between the VIS and IR-detectors.

To quantify these systematic errors, we follow the polarization state of the electromagnetic radiation from the laser source to the light detector. The incident Stokes vector can be described by a vector in the Poincare sphere describing all possible polarization states by its longitude 2χ and latitude 2ω [54]. These angles, which quantify the deviation from considered incident polarization states $\pi = (p, 45+, RC)$, modify $a_{\pi}(\lambda)$ to $d_{\pi}(\lambda)$ coefficients (i.e. Eqs. (5) no longer apply). To minimize this remaining ellipticity, two successive PBC have been used to precisely set the polarization state of the incident radiation at wavelength λ to (p) , then $(45+, RC)$ using wave-plates. On the detector side, as the retro-reflecting PBC is imperfect ($R_s > 99.5\%$, $T_p > 90\%$), the fraction $R_s T_p$ of the s -polarization component of the light intensity is measured, together with an undesired fraction $R_p T_s$ originating from the p -component of the scattered radiation. To minimize this polarization cross-talk $CT = R_p T_s / R_s T_p$ and allow the s -polarization component of the scattered radiation to be detected (with efficiency T_p), a second PBC has been inserted in the detector after the retro-reflecting PBC. Likewise, wavelength cross-talks between the VIS and IR-detectors have been minimized by using narrow interference filters at wavelengths λ_{VIS} and λ_{IR} , presenting an optical density of 5 at the complementary wavelength (i.e. at wavelength λ_{VIS} for the λ_{IR} -polarimeter). To be quantitative, we quantified the error in $\Delta f_{ij}(\lambda)$ on $f_{ij}(\lambda)$ at first order in $\chi(\lambda)$, $\omega(\lambda)$ and $CT(\lambda)$:

$$\Delta f_{33}(\lambda) = 2\omega f_{34} + 2CT f_{33} \quad (6a)$$

$$\Delta f_{44}(\lambda) = 2\chi f_{34} + 2CT f_{44} \quad (6b)$$

$$\Delta f_{12}(\lambda) = 2\omega f_{22} + 2CT f_{12} \quad (6c)$$

$$\Delta f_{34}(\lambda) = 2\chi f_{33} - 2CT f_{34} \quad (6d)$$

$$\Delta f_{22}(\lambda) = 5CTf_{22}/[2(f_{12} + 1) + 3CT] \quad (6e)$$

Where, to ease the reading, the wavelength dependence of $\chi(\lambda)$, $\omega(\lambda)$ and $CT(\lambda)$ has been omitted. Following Eqs. (6), at negligible polarization cross-talk, the error on $f_{ij}(\lambda)$ is majored by $2\chi(\lambda)$ or $2\omega(\lambda)$ since $f_{ij}(\lambda)$ are below unity. The error on $f_{44}(\lambda)$ is then at most equal to $2\chi(\lambda)$. Fig. 2 displays in dashed lines the variation of the detected scattered intensity when considering a 2° deviation in both $\chi(\lambda)$ and $\omega(\lambda)$ assuming negligible polarization cross-talk. As to be seen in Fig.2(a) minima, the error on $f_{22}(\lambda)$ is independent from $\chi(\lambda)$ and $\omega(\lambda)$. Moreover, when $f_{34}(\lambda) = 0.05$ and $f_{33}(\lambda) = -0.4$, a 1 %-relative accuracy is achieved on $f_{33}(\lambda)$ (resp. $f_{44}(\lambda)$) if $\omega(\lambda)$ (resp. $\chi(\lambda)$) remains below 2.3° . The angles $\chi(\lambda)$ and $\omega(\lambda)$ can be precisely evaluated in our experiment by taking benefit from complementary polarization states (45-) and (LC) since $2\chi(\lambda) = a_{45+}/(a_{45+} + c_{45+}) - a_{45-}/(a_{45-} + c_{45-})$ while $2\omega(\lambda) = a_{RC}/(a_{RC} + c_{RC}) - a_{LC}/(a_{LC} + c_{LC})$.

3. Ragweed pollen samples

3.1. *Ambrosia artemisiifolia* pollen

Our ragweed (*Ambrosia artemisiifolia*) samples are from Stallergenes Greer supplier. Dry ragweed powder has been embedded in laboratory ambient air using a solid pollen generator supplied with dried compressed air (RH < 10 %), before injecting the ragweed pollens grains in the light scattering volume as schemed in Fig. 1. The size and the shape of our ragweed samples have been characterized as detailed below. Less than 5 % fluctuations in the ragweed pollen number concentration were observed in the coarse mode of the size distribution. In complement, to validate the ability of the λ_{IR} -laboratory polarimeter to precisely evaluate scattering matrices, spherical water droplets, which follow Mie theory, have also been embedded in ambient air using a commercial atomizer.

3.2. Ragweed pollen particles scanning electron microscopic images

To characterize the size and the shape of pollens, scanning electron microscopy (SEM) was used, following the historical methodology [20]. Since pollen are dielectric material, to apply SEM, the ragweed pollen particles were deposited on an adhesive SEM tape, metallized with thin copper coating to increase the conductivity of the grains' surface. Fig. 3 presents our scanning electron microscope images, observed with a magnification factor of 3250 (panel (a), then 10 000 (panel b) to highlight the surface roughness of the pollen membrane. In agreement with the literature [19], our ragweed samples exhibit a volume equivalent diameter of $21 \mu\text{m}$ and an overall spherical shape, covered by regular spikes (echinus) of about $1 \mu\text{m}$ length. One of the three characteristic black apertures of ragweed, which are smaller than $2 \mu\text{m}$, is visible at the pollen wall in the lower part of Fig. 3(a). In agreement with the literature, this pollen wall exhibits a perforate structure, i.e. covered with around 100 nm diameter holes to be seen in Fig. 3(b).

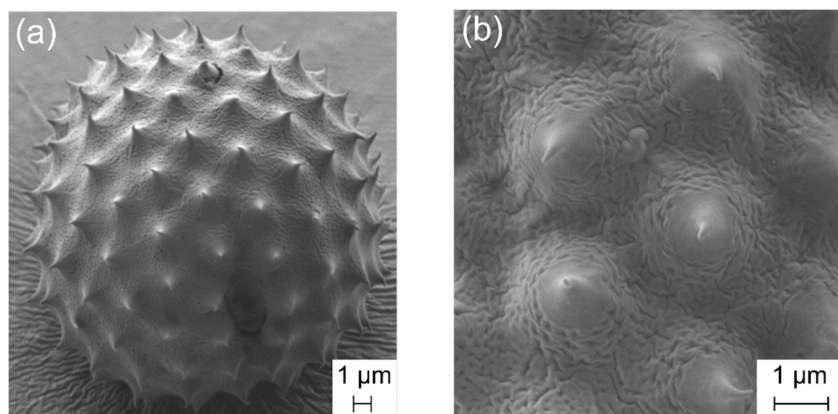


Fig. 3. Scanning electron microscopy (SEM) images of our *Ambrosia Artemisiifolia* samples embedded in ambient air, once deposited on an adhesive substrate with a 3250 magnification (a), 10 000 magnification (b). One of the three characteristic black apertures is visible in panel (a), while the surface roughness to be seen in panel (b) corresponds to around 100 nm diameter holes.

3.3. Ragweed pollen particles size distribution

To evaluate the size of our ragweed samples, in complement to the above SEM images, an aerodynamic particle sizer (APS) was used. This commercial instrument evaluates the aerodynamic diameter through a time-of-flight measurement. Fig. 4(a) presents the retrieved ragweed size distribution, which exhibits a coarse mode at seventeen micrometres, but also finer particles attributed to sub-pollen particles [55]. The aerodynamic diameter can be lower than the volume equivalent diameter since ragweed pollen grains are non-spherical and exhibit a dynamic shape factor above unity [56]. Likewise, the size distribution of our spherical water droplets embedded in ambient air was measured with a scanning mobility particle sizer coupled to an optical particle sizer, as displayed in Fig. 4(b).

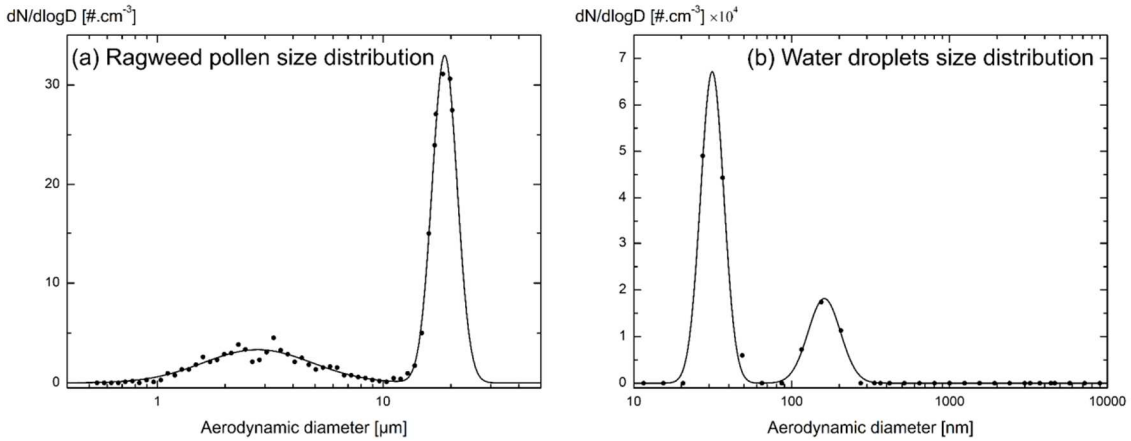


Fig. 4. (a) Particle size distribution of our generated ragweed pollen particles, as measured with an aerodynamic particle sizer (upper measured size equal to 20 μm). (b) Particle size distribution of water droplets to be used in Section 4.1 to validate the λ_{IR} -laboratory polarimeter.

4. Results and discussion

Following Sections 2 and 3, the scattering matrix of ragweed pollen is evaluated in laboratory at wavelengths $(\lambda_{VIS}, \lambda_{IR})$ with corresponding error bars. The $(\lambda_{VIS}, \lambda_{IR})$ -polarimeters are first validated on spherical water droplets that follow the analytical Lorenz-Mie theory.

4.1. (VIS, IR) experimental set-up validation on spherical water droplets

By applying Fig. 1 experimental set-up on spherical water droplets, we recorded the variations of the detected scattered intensity $I_{\pi}(\lambda, \psi)$ for successive incident polarization states $\pi = (p, 45+, RC)$ at wavelength λ_{VIS} in Fig. 5(a) and wavelength λ_{IR} in Fig. 5(b). To account for potential particles number fluctuations, the detected scattered intensity has been normalized by that of a polarization insensitive photodetector. At both wavelengths, the (p) -polarization curve exhibits null minima, consistent with spherical particles for which $f_{22}(\lambda) = 1$. Similarly, in the $(45+)$ -polarization curve, the difference between two successive minima is not distinguishable, meaning that $f_{34}(\lambda)$ is very close to zero for our spherical particles. For each incident polarization state $\pi = (p, 45+, RC)$, coefficients from $a_{\pi}(\lambda)$ to $d_{\pi}(\lambda)$ are evaluated by adjusting the experimental data points with Eqs (5) to provide the scattering matrix presented in Table 1 at both wavelengths with corresponding error bars. Indeed, use of complementary incident polarization states $\pi = (s, 45-, LC)$ allowed to evaluate $2\omega = 2\chi = 0.01$ at both wavelengths. Within our experimental error bars, the retrieved normalized scattering matrix elements agree with numerically exact solutions the Maxwell's equations, obtained by applying the Lorenz-Mie theory [49], which provides $f_{22}(\lambda) = -f_{33}(\lambda) = -f_{44}(\lambda) = 1$ and $f_{12}(\lambda) = f_{34}(\lambda) = 0$ for the size distribution shown in Fig. 4(b) by taking into account the complex refractive index of water at both wavelengths. Hence, the newly-developed $(\lambda_{VIS}, \lambda_{IR})$ -polarimeters precisely reveal the scattering matrix of spherical water droplets embedded in ambient air at two both wavelengths.

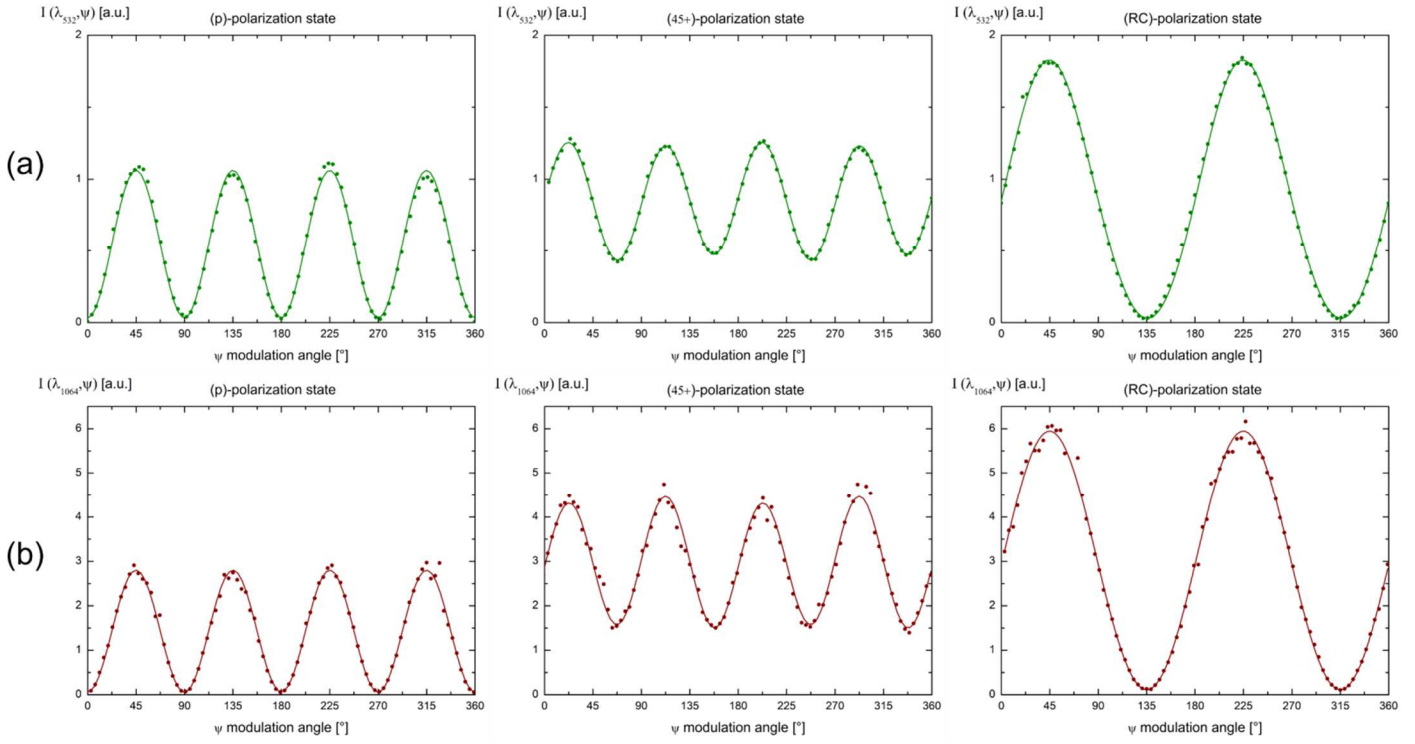


Fig. 5. Detected light intensity $I_{\pi}(\lambda, \psi)$ scattered by water droplets as a function of the modulation angle ψ of the QWP at wavelength λ_{VIS} (panel (a), data in green) and wavelength λ_{IR} (panel (b), data in red) for successive incident polarization states $\pi = (p, 45+, RC)$ at 178° scattering angle. The detected scattered intensity, expressed in arbitrary units (a.u.) as $P_0(\lambda)$ is wavelength dependent, is adjusted with Eq. (4) to retrieve the scattering matrix elements $f_{ij}(\lambda) = F_{ij}(\lambda)/F_{11}(\lambda)$ using Eqs. (5).

Table 1

$(\lambda_{VIS}, \lambda_{IR})$ -evaluation of the scattering matrix elements $f_{ij}(\lambda) = F_{ij}(\lambda)/F_{11}(\lambda)$ for spherical water droplets at 178° scattering angle, retrieved by adjusting the Fig. 5 experimental data points with Eqs. (5).

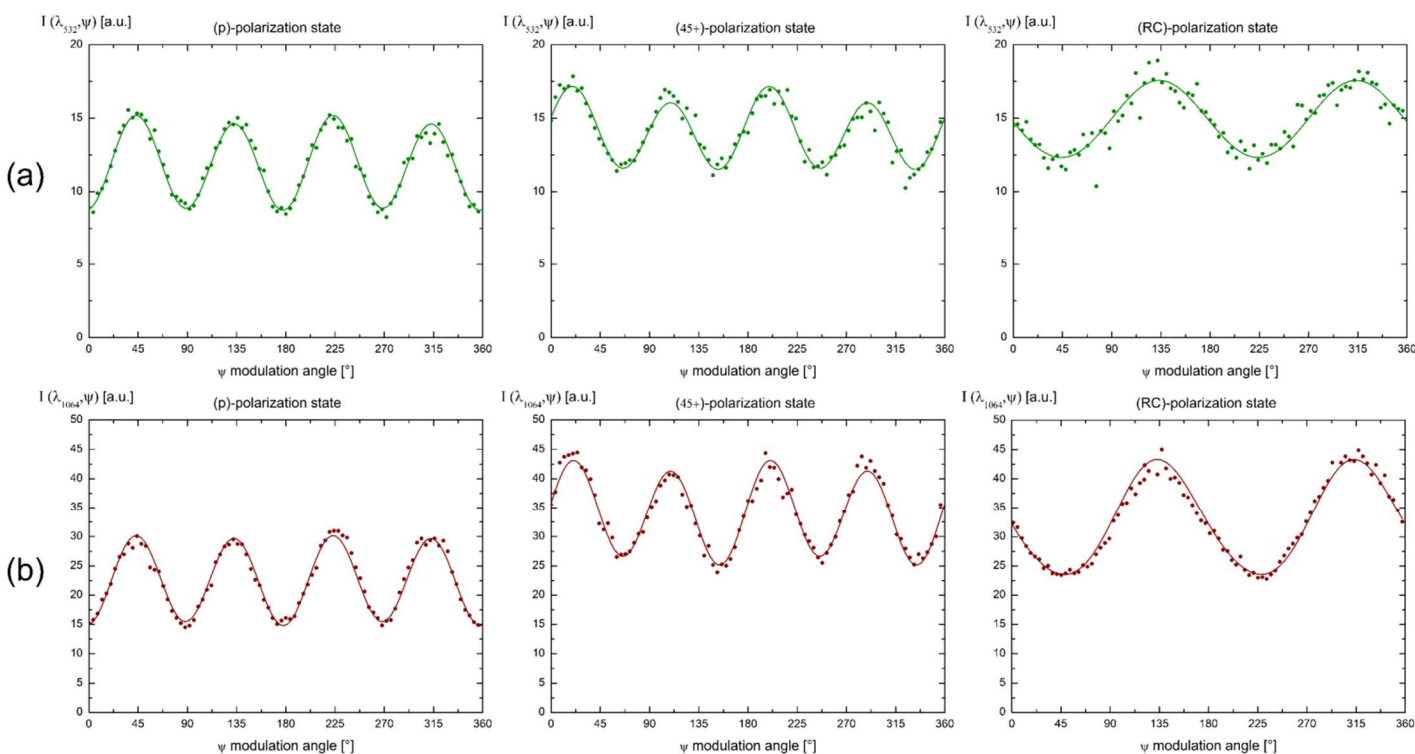
VIS-wavelength ($\lambda_{VIS} = 532$ nm)				IR-wavelength ($\lambda_{IR} = 1064$ nm)			
1	-0.01 ± 0.02	0	0	1	0.01 ± 0.03	0	0
-0.01 ± 0.02	0.97 ± 0.02	0	0	0.01 ± 0.03	0.99 ± 0.04	0	0
0	0	-0.94 ± 0.02	-0.02 ± 0.02	0	0	-0.97 ± 0.04	0.02 ± 0.02
0	0	0.02 ± 0.02	-0.98 ± 0.02	0	0	-0.02 ± 0.02	-0.97 ± 0.02

4.2. Spectral dependence of the scattering matrix elements of ragweed

Fig. 6 is the analogue of Fig. 5 but dedicated to ragweed pollen particles. In contrary to Section 4.1, the minima in the (p)-polarization curve (left panel), which are related to the scattering matrix element $1 - f_{22}(\lambda)$, no longer vanish, in agreement with the ragweed overall nonspherical shape. Likewise, the minima in the (RC)-polarization curve (right panel) are constant and related to the scattering matrix element $1 - f_{44}(\lambda)$. In the (45+)-polarization curve (middle panel), at wavelength λ_{IR} , a difference exists between two successive local minima or maxima, meaning that $f_{34}(\lambda_{IR})$ is non-zero for ragweed pollen particles, as for several biological species [31]. As for water droplets in Fig. 5, the reproducibility of these extrema is clearly observed in Fig. 6, which means that the size and the shape distribution of our ragweed samples did not vary during the experimental acquisition. Coefficients $a_{\pi}(\lambda)$ to $d_{\pi}(\lambda)$ were then retrieved by adjusting our experimental data points at both wavelengths ($\lambda_{VIS}, \lambda_{IR}$) with Eq. (4) to retrieve the normalized scattering matrix elements $f_{ij}(\lambda)$ presented in Table 2 by applying Eq. (5). The conditions of applicability of the single-scattering approximation may there be questioned. Mishchenko et al. [57] underscored that for the SSA to be applicable, a large average inter-particle distance $\langle d \rangle$ (i.e. $k_1 \langle d \rangle \gg 30$, where k_1 is the wave vector in the surrounding medium) and low particle volume concentrations ρ (low packing densities $\rho \ll 1$ %) should

325
326
327
328
329
330
331
332
333
334
335
336
337
338
339
340

be considered. In our laboratory light scattering experiment, from the ragweed particles size distribution shown in Fig. 4, we calculate a particle volume concentration of $\rho = 3.9 \times 10^{-8} \ll 1$. Moreover, according to [58], at volume fraction ρ , the mean distance between neighbour particles for monodisperse particles with radius r is $\langle d \rangle = 0.554 \times (4\pi/(3\rho))^{1/3} r$. Even if one considers $\rho = 3.9 \times 10^{-6}$, monodisperse grains with effective radius $r = 10.5 \mu\text{m}$ correspond to $\langle d \rangle = 0.6 \text{ mm}$, which leads to $k_1 \langle d \rangle \approx 7000 \gg 30$. As a result, the single-scattering approximation is fairly safe in our laboratory experiment where the particles are moving in a thin (2.5 mm) wide beam, so that the volume element is optically thin. The error bars in Table 2 result from the evaluation of $2\omega(\lambda_{VIS}) = 0.03$ and $2\chi(\lambda_{VIS}) = 0.02$, and $2\omega(\lambda_{IR}) = 2\chi(\lambda_{IR}) = 0.01$. Interestingly, our error bars remain lower than the observed spectral variations of the scattering matrix elements. Hence, due to negligible wavelength cross-talks, the spectral dependence of the ragweed scattering matrix elements is revealed within our experimental error bars : the diagonal scattering matrix elements $f_{22}(\lambda)$, $f_{33}(\lambda)$ and $f_{44}(\lambda)$ are larger at wavelength λ_{IR} than at wavelength λ_{VIS} . Equally, the off-diagonal element $f_{34}(\lambda)$ increases from λ_{VIS} to λ_{IR} , except for $f_{12}(\lambda)$, which exhibits no spectral variation between both wavelengths λ_{VIS} and λ_{IR} . As a conclusion, the retrieved scattering matrix elements presented in Table 2 provide precise spectral and polarimetric fingerprints of ragweed pollen.



341
342
343
344
345
346

Fig. 6. Same as Fig. 5 for ragweed pollen particles.

Table 2

Same as Table 1 for ragweed pollen particles.

VIS-wavelength ($\lambda_{VIS} = 532 \text{ nm}$)				IR-wavelength ($\lambda_{IR} = 1064 \text{ nm}$)			
1	0.01 ± 0.04	0	0	1	0.02 ± 0.01	0	0
0.01 ± 0.04	0.40 ± 0.01	0	0	0.02 ± 0.01	0.48 ± 0.01	0	0
0	0	-0.35 ± 0.06	0.00 ± 0.04	0	0	-0.48 ± 0.02	0.05 ± 0.02
0	0	-0.00 ± 0.04	-0.18 ± 0.03	0	0	-0.05 ± 0.02	-0.29 ± 0.02

347
348
349
350
351
352
353

To interpret the observed spectral dependence of ragweed scattering matrix elements, two main arguments can be put forward. Firstly, the ragweed complex refractive index is a priori wavelength dependent, though the literature is, to our knowledge, not well documented, especially at wavelength λ_{IR} . At wavelength λ_{VIS} , values of the Pinus refractive index between 1.50 and 1.53 have been reported [59] using optical diffraction tomography and similar values were obtained for the refractive index of the cell of a yew pollen grain [60]. Secondly, ragweed pollen grains are large-sized particles and present periodic

354 structures, the interference of waves scattered by the large particle surface and the spikes may appear,,
355 which may play a role in the observed spectral dependence of the scattering matrix elements. Also, the
356 interference of waves scattered by different spikes may also reveal itself in the phase and spectral
357 dependences of the scattering matrix elements. It is however far beyond the scope of this paper to
358 investigate these possible explanations. Still as is, our retrieved scattering matrix elements may interest the
359 light scattering numerical community for ragweed pollen grains exhibit fairly large size parameters (around
360 120 at wavelength λ_{VIS}) and are beyond the reach of numerically exact light-scattering methods. Light
361 scattering by ragweed is a priori difficult to model numerically as ragweed pollen particles are complex-
362 shaped particles with regular spikes, apertures, holes and surface roughness. As underscored by M.
363 Kahnert et al. [61] in their review on model particles in atmospheric optics, several numerical approaches
364 have been considered to evaluate light scattering by complex-shaped particles. Very recently, D. Petrov
365 [50] applied the T-matrix numerical code on coronavirus-shaped particles which exhibit characteristic
366 spikes, as for ragweed. Applying this new numerical method to ragweed pollen particles is interesting but a
367 priori challenging due to their larger size [62,63]. To account for surface roughness, the size parameter
368 (micrometer range, wavelength λ_{VIS}) is too small for applying geometrical optics, but geometrical optics
369 may eventually be used in conjunction with a random-tilting method (M. Kahnert, private communication),
370 as successfully applied for large ice particles presenting surface roughness [64]. These considerations
371 underscore the complexity of a precise numerical modelling of light scattering by ragweed pollen particles,
372 which further reinforce the importance of controlled-laboratory experiments allowing to precisely retrieve the
373 ragweed scattering matrix at wavelengths ($\lambda_{VIS}, \lambda_{IR}$). Hence, to tackle the important issue of light scattering
374 by large and complex-shaped particles, more laboratory work has to be proposed, at other scattering
375 angles and at other laser wavelengths. Still as is, our retrieved scattering matrices may help to constrain
376 such light scattering numerical models.

377 5. Conclusion and outlooks

378 In this paper, a controlled-laboratory experiment is proposed to precisely evaluate the scattering matrix of
379 ragweed pollen particles embedded in ambient air. Ragweed pollen, or *Ambrosia artemisiifolia*, is indeed
380 one of the major pollens whose impact on public health and on the Earth's climate is appealed to increase
381 in the forthcoming decades, due to global warming. In this context, the goal of this paper is to improve the
382 knowledge on this important pollen, by quantifying its ability to scatter light at two wavelengths. This task is
383 complex as ragweed is beyond the reach of numerically exact light scattering models, due its tens of
384 micrometres size. Moreover, the shape of ragweed pollen particles is also complex, with a small-scale non-
385 spherical feature exhibiting spikes, apertures and holes, as observed in Section 3 with scanning electron
386 microscopy. To face such a complexity, we took benefit in Section 2 from the scattering matrix formalism to
387 build a controlled-laboratory experiment, based on two polarimeters, allowing precise evaluation of the
388 ragweed scattering matrix at two wavelengths, in the visible and infra-red spectral ranges. The infra-red
389 spectral range was chosen to account for the large size of ragweed pollen particles and the newly-built
390 polarimeter at wavelength λ_{IR} has been validated on spherical water droplets following Lorenz-Mie theory.
391 Then, the polarimeters were operated on ragweed pollen particles embedded in ambient air. Special care
392 has been taken to evaluate the systematic and statistical uncertainties on the retrieved scattering matrix
393 elements by taking into account potential polarization and wavelength cross-talks. Interestingly, our
394 experimental error bars are sufficiently low to reveal the spectral dependence of the ragweed scattering
395 matrix: all ragweed scattering matrix elements except f_{12} are higher at wavelength λ_{IR} than at wavelength
396 λ_{VIS} . As a result, precise spectral and polarimetric ragweed fingerprints are here provided.

397 The outlooks of this work are numerous. First of all, the ragweed scattering matrix elements may also be
398 evaluated in the UV-spectral range to improve our sensitivity to the small-scale irregularities exhibited at the
399 ragweed grains' surface. Moreover, evaluating the ragweed scattering matrix elements at wavelengths
400 larger than 1 μm would ensure the size parameters of the ragweed spikes to be within 1 or 2. As
401 underscored in several papers [65–67], the features of exactly these sizes are responsible for characteristic
402 details in the phase and spectral dependences of the intensity and polarization. We may also extend this
403 evaluation to other scattering angles, including exact backscattering for remote sensing observations. Our
404 laboratory experimental set-up allows scattering angles measurements from 176.0° to 180.0° [53] and the
405 dependence of the ragweed scattering matrix elements with the scattering angle will be studied in a
406 dedicated contribution, as this question may provide important information on the object under study itself
407 [68]. Addressing the phase function would also be interesting but challenging within our experimental set-
408 up [53]. As well, other pollens can be likewise studied by applying the same methodology to investigate
409 how light scattering is modified by different grain morphologies. Finally, our laboratory findings can be

410 applied by the light scattering numerical community to further improve their numerical models by
411 investigating complex-shaped particles with spikes such as ragweed, or even coronavirus as recently
412 tackled by [50]. Indeed, the near but non-spherical overall ragweed shape, with regular spikes, bears
413 resemblances with that of other biological particles. Hence, our methodology may be potentially applied to
414 study such biological objects. This however represents a laboratory intensive work. Still, precise modelling
415 of light scattering by ragweed represents a challenging task due to its large size and complex shape. We
416 hope our experimental contribution at two wavelengths will help to further tackle the important issue of the
417 light scattering by complex-shaped and large particles.

418 **Acknowledgments**

419 CNRS is acknowledged for financial support and the Lyon Centre Technologique des Microstructures for
420 their help in electronic microscopy.
421

422 **References**

- 423
- 424 1. E. A. Taketomi, M. C. Sopenete, P. F. de Sousa Moreira, and F. de Assis Machado Vieira, "Pollen allergic
425 disease: pollens and its major allergens," *Braz. J. Otorhinolaryngol.* **72**(4), 562–567 (2006).
- 426 2. P. Tamarcaz, C. Lambelet, B. Clot, C. Keimer, and C. Hauser, "Ragweed (Ambrosia) progression and
427 its health risks: will Switzerland resist this invasion?," *SWISS MED WKLY* **12** (2005).
- 428 3. C. Bohren, "Ambrosia artemisiifolia – a motivation for European-wide control," **6** (2008).
- 429 4. M. Smith, L. Cecchi, C. A. Skjøth, G. Karrer, and B. Šikoparija, "Common ragweed: A threat to
430 environmental health in Europe," *Environ. Int.* **61**, 115–126 (2013).
- 431 5. M. Thibaudon, B. Šikoparija, G. Oliver, M. Smith, and C. A. Skjøth, "Ragweed pollen source inventory
432 for France – The second largest centre of Ambrosia in Europe," *Atmos. Environ.* **83**, 62–71 (2014).
- 433 6. U. Schaffner, S. Steinbach, Y. Sun, C. A. Skjøth, L. A. de Weger, S. T. Lommen, B. A. Augustinus, M.
434 Bonini, G. Karrer, B. Šikoparija, M. Thibaudon, and H. Müller-Schärer, "Biological weed control to
435 relieve millions from Ambrosia allergies in Europe," *Nat. Commun.* **11**(1), 1–7 (2020).
- 436 7. H. Behrendt and W.-M. Becker, "Localization, release and bioavailability of pollen allergens: the
437 influence of environmental factors," **7** (n.d.).
- 438 8. D. Myszkowska, "Aerobiological studies – current state and future challenges," *Alergoprofil* **16**(1), 8–
439 14 (2020).
- 440 9. F. D. Pope, "Pollen grains are efficient cloud condensation nuclei," *Environ. Res. Lett.* **5**(4), 044015
441 (2010).
- 442 10. M. C. Wozniak, F. Solmon, and A. L. Steiner, "Pollen Rupture and Its Impact on Precipitation in Clean
443 Continental Conditions," *Geophys. Res. Lett.* **45**(14), 7156–7164 (2018).
- 444 11. E. Gute and J. P. D. Abbatt, "Ice nucleating behavior of different tree pollen in the immersion mode,"
445 *Atmos. Environ.* **231**, 117488 (2020).
- 446 12. D. Spänkuch, W. Döhler, and J. Güldner, "Effect of coarse biogenic aerosol on downwelling infrared
447 flux at the surface," *J. Geophys. Res. Atmospheres* **105**(D13), 17341–17350 (2000).
- 448 13. T. Mang, F. Essl, D. Mosef, and S. Dullinger, "Climate warming drives invasion history of Ambrosia
449 artemisiifolia in central Europe," *Preslia* **90**(1), 59–81 (2018).
- 450 14. P. Wayne, S. Foster, J. Connolly, F. Bazzaz, and P. Epstein, "Production of allergenic pollen by ragweed
451 (*Ambrosia artemisiifolia* L.) is increased in CO₂-enriched atmospheres," *Ann. Allergy. Asthma.*
452 *Immunol.* **88**(3), 279–282 (2002).
- 453 15. L. Ziska, K. Knowlton, C. Rogers, D. Dalan, N. Tierney, M. A. Elder, W. Filley, J. Shropshire, L. B. Ford, C.
454 Hedberg, P. Fleetwood, K. T. Hovanky, T. Kavanaugh, G. Fulford, R. F. Vrtis, J. A. Patz, J. Portnoy, F.
455 Coates, L. Bielory, and D. Frenz, "Recent warming by latitude associated with increased length of
456 ragweed pollen season in central North America," *Proc. Natl. Acad. Sci.* **108**(10), 4248–4251 (2011).
- 457 16. M. Sofiev, J. Belmonte, R. Gehrig, R. Izquierdo, M. Smith, Å. Dahl, and P. Siljamo, "Airborne Pollen
458 Transport," in *Allergenic Pollen*, M. Sofiev and K.-C. Bergmann, eds. (Springer Netherlands, 2013), pp.
459 127–159.

- 460 17. L. Makra, I. Matyasovszky, M. Thibaudon, and M. Bonini, "Forecasting ragweed pollen characteristics
461 with nonparametric regression methods over the most polluted areas in Europe," *Int. J. Biometeorol.*
462 **55**(3), 361–371 (2011).
- 463 18. K. Zink, P. Kaufmann, B. Petitpierre, O. Broennimann, A. Guisan, E. Gentilini, and M. W. Rotach,
464 "Numerical ragweed pollen forecasts using different source maps: a comparison for France," *Int. J.*
465 *Biometeorol.* **61**(1), 23–33 (2017).
- 466 19. R. R. Robbins, D. B. Dickinson, and A. M. Rhodes, "Morphometric Analysis of Pollen from Four Species
467 of *Ambrosia* (compositae)," *Am. J. Bot.* **66**(5), 538–545 (1979).
- 468 20. M. Hesse, ed., *Pollen Terminology: An Illustrated Handbook* (Springer, 2009).
- 469 21. C. Liu and Y. Yin, "Inherent optical properties of pollen particles: a case study for the morning glory
470 pollen," *Opt. Express* **24**(2), A104 (2016).
- 471 22. J. M. Hirst, "An automatic volumetric spore trap," *Ann. Appl. Biol.* **39**(2), 257–265 (1952).
- 472 23. A. Daood, E. Ribeiro, and M. Bush, "Pollen Grain Recognition Using Deep Learning," in *Advances in*
473 *Visual Computing*, G. Bebis, R. Boyle, B. Parvin, D. Koracin, F. Porikli, S. Skaff, A. Entezari, J. Min, D.
474 Iwai, A. Sadagic, C. Scheidegger, and T. Isenberg, eds., *Lecture Notes in Computer Science* (Springer
475 International Publishing, 2016), pp. 321–330.
- 476 24. Y.-L. Pan, S. C. Hill, R. G. Pinnick, J. M. House, R. C. Flagan, and R. K. Chang, "Dual-excitation-
477 wavelength fluorescence spectra and elastic scattering for differentiation of single airborne pollen
478 and fungal particles," *Atmos. Environ.* **45**(8), 1555–1563 (2011).
- 479 25. D. Kiselev, L. Bonacina, and J.-P. Wolf, "A flash-lamp based device for fluorescence detection and
480 identification of individual pollen grains," *Rev. Sci. Instrum.* **84**(3), 033302 (2013).
- 481 26. T. Könnemann, N. Savage, T. Klimach, D. Walter, J. Fröhlich-Nowoisky, H. Su, U. Pöschl, J. A. Huffman,
482 and C. Pöhlker, "Spectral Intensity Bioaerosol Sensor (SIBS): an instrument for spectrally resolved
483 fluorescence detection of single particles in real time," *Atmospheric Meas. Tech.* **12**(2), 1337–1363
484 (2019).
- 485 27. R. Giri, C. Morello, Y. W. Heinson, O. Kempainen, G. Videen, G. Videen, G. Videen, and M. J. Berg,
486 "Generation of aerosol-particle light-scattering patterns from digital holograms," *Opt. Lett.* **44**(4),
487 819–822 (2019).
- 488 28. E. Sauvageat, Y. Zeder, K. Auderset, B. Calpini, B. Clot, B. Crouzy, T. Konzelmann, G. Lieberherr, F.
489 Tummon, and K. Vasilatou, "Real-time pollen monitoring using digital holography," *Atmospheric*
490 *Meas. Tech.* **13**(3), 1539–1550 (2020).
- 491 29. M. J. Berg and G. Videen, "Digital holographic imaging of aerosol particles in flight," *J. Quant.*
492 *Spectrosc. Radiat. Transf.* **112**(11), 1776–1783 (2011).
- 493 30. W. S. Bickel, J. F. Davidson, D. R. Huffman, and R. Kilkson, "Application of polarization effects in light
494 scattering: a new biophysical tool.," *Proc. Natl. Acad. Sci.* **73**(2), 486–490 (1976).
- 495 31. W. S. Bickel and M. E. Stafford, "Biological Particles as Irregularly Shaped Scatterers," in *Light*
496 *Scattering by Irregularly Shaped Particles* (Springer, Boston, MA, 1980), pp. 299–305.
- 497 32. P. M. A. Sloot, A. G. Hoekstra, H. van der Liet, and C. G. Figdor, "Scattering matrix elements of
498 biological particles measured in a flow through system: theory and practice," *Appl. Opt.* **28**(10), 1752
499 (1989).
- 500 33. M. Surbek, C. Esen, G. Schweiger, and A. Ostendorf, "Pollen characterization and identification by
501 elastically scattered light," *J. Biophotonics* **4**(1–2), 49–56 (2011).
- 502 34. T. Iwai, "Polarization Analysis of Light Scattered by Pollen Grains of *Cryptomeria japonica*," *Jpn. J.*
503 *Appl. Phys.* **52**(6R), 062404 (2013).
- 504 35. P. Raman, K. A. Fuller, and D. A. Gregory, "Polarization signatures of airborne particulates," *Opt. Eng.*
505 **52**(7), 074106 (2013).
- 506 36. S. A. Nouri, D. A. Gregory, and K. Fuller, "Development of an angle-scanning spectropolarimeter:
507 Preliminary results," *J. Quant. Spectrosc. Radiat. Transf.* **206**, 342–354 (2018).
- 508 37. S. Matsuda and S. Kawashima, "Relationship between laser light scattering and physical properties of
509 airborne pollen," *J. Aerosol Sci.* **124**, 122–132 (2018).

- 510 38. S. Holler, S. D. Fuerstenau, and C. R. Skelsey, "Simultaneous two-color, two-dimensional angular
511 optical scattering patterns from airborne particulates: Scattering results and exploratory analysis," J.
512 Quant. Spectrosc. Radiat. Transf. **178**, 167–175 (2016).
- 513 39. M. I. Mishchenko, L. D. Travis, and A. A. Lacis, *Scattering, Absorption, and Emission of Light by Small*
514 *Particles* (Cambridge University Press, 2002).
- 515 40. G. Roy, "Lidar polarization discrimination of bioaerosols," Opt. Eng. **49**(11), 116201 (2010).
- 516 41. M. Sicard, R. Izquierdo, M. Alarcón, J. Belmonte, A. Comerón, and J. M. Baldasano, "Near-surface and
517 columnar measurements with a micro pulse lidar of atmospheric pollen in Barcelona, Spain,"
518 Atmospheric Chem. Phys. **16**(11), 6805–6821 (2016).
- 519 42. K. Sassen, "Boreal tree pollen sensed by polarization lidar: Depolarizing biogenic chaff," Geophys. Res.
520 Lett. **35**(18), (2008).
- 521 43. Y. M. Noh, D. Müller, H. Lee, and T. J. Choi, "Influence of biogenic pollen on optical properties of
522 atmospheric aerosols observed by lidar over Gwangju, South Korea," Atmos. Environ. **69**, 139–147
523 (2013).
- 524 44. A. Miffre, G. David, B. Thomas, and P. Rairoux, "Atmospheric non-spherical particles optical properties
525 from UV-polarization lidar and scattering matrix," Geophys. Res. Lett. **38**(16), L16804 (2011).
- 526 45. T. Mehri, O. Kemppinen, G. David, H. Lindqvist, J. Tynnelä, T. Nousiainen, P. Rairoux, and A. Miffre,
527 "Investigating the size, shape and surface roughness dependence of polarization lidars with light-
528 scattering computations on real mineral dust particles: Application to dust particles' external mixtures
529 and dust mass concentration retrievals," Atmospheric Res. **203**, 44–61 (2018).
- 530 46. A. Hoekstra, ed., *Optics of Biological Particles: Proceedings of the NATO Advanced Research Workshop*
531 *on Fluorescence and Other Optical Properties of Biological Particles for Biological Warfare Agent*
532 *Sensors, Novosibirsk, Russia, 3 - 6 October 2005*, NATO Science Series Series II, Mathematics, Physics
533 and Chemistry No. 238 (Springer, 2007).
- 534 47. D. Mackowski, L. Kolokolova, and W. Sparks, "T-matrix approach to calculating circular polarization of
535 aggregates made of optically active materials," J. Quant. Spectrosc. Radiat. Transf. **112**(11), 1726–
536 1732 (2011).
- 537 48. R. A. Meyer, "Light scattering from biological cells: dependence of backscatter radiation on
538 membrane thickness and refractive index," Appl. Opt. **18**(5), 585 (1979).
- 539 49. C. F. Bohren and D. R. Huffman, *Absorption and Scattering of Light by Small Particles* (Wiley-VCH,
540 1983).
- 541 50. D. Petrov, "Photopolarimetric properties of coronavirus model particles: Spike proteins number
542 influence," J. Quant. Spectrosc. Radiat. Transf. **248**, 107005 (2020).
- 543 51. M. I. Mishchenko, "Electromagnetic scattering by nonspherical particles: A tutorial review," J. Quant.
544 Spectrosc. Radiat. Transf. **110**(11), 808–832 (2009).
- 545 52. J. W. Hovenier, C. Van Der Mee, and H. Domke, *Transfer of Polarized Light in Planetary Atmospheres*,
546 *Astrophysics and Space Science Library* (Springer Netherlands, 2004), **318**.
- 547 53. A. Miffre, D. Cholleton, and P. Rairoux, "Laboratory evaluation of the scattering matrix elements of
548 mineral dust particles from 176.0° up to 180.0°-exact backscattering angle," J. Quant. Spectrosc.
549 Radiat. Transf. **222–223**, 45–59 (2019).
- 550 54. W. A. Shurcliff, *Polarized Light: Production and Use* (1962).
- 551 55. A. Bacsi, B. Choudhury, N. Dharajiya, S. Sur, and I. Boldogh, "Subpollen particles: Carriers of allergenic
552 proteins and oxidases," J. Allergy Clin. Immunol. **118**(4), 844–850 (2006).
- 553 56. P. F. DeCarlo, J. G. Slowik, D. R. Worsnop, P. Davidovits, and J. L. Jimenez, "Particle Morphology and
554 Density Characterization by Combined Mobility and Aerodynamic Diameter Measurements. Part 1:
555 Theory," Aerosol Sci. Technol. **38**(12), 1185–1205 (2004).
- 556 57. M. I. Mishchenko, L. Liu, and G. Videen, "Conditions of applicability of the single-scattering
557 approximation," Opt. Express **15**(12), 7522 (2007).
- 558 58. P. P. Bansal and A. J. Ardell, "Average nearest-neighbor distances between uniformly distributed finite
559 particles," Metallography **5**(2), 97–111 (1972).

- 560 59. G. Kim, S. Lee, S. Shin, and Y. Park, "Three-dimensional label-free imaging and analysis of Pinus pollen
561 grains using optical diffraction tomography," *Sci. Rep.* **8**(1), (2018).
- 562 60. F. Charrière, A. Marian, F. Montfort, J. Kuehn, T. Colomb, E. Cuhe, P. Marquet, and C. Depeursinge,
563 "Cell refractive index tomography by digital holographic microscopy," *Opt. Lett.* **31**(2), 178 (2006).
- 564 61. M. Kahnert, T. Nousiainen, and H. Lindqvist, "Review: Model particles in atmospheric optics," *J.*
565 *Quant. Spectrosc. Radiat. Transf.* **146**, 41–58 (2014).
- 566 62. D. Petrov, Y. Shkuratov, and G. Videen, "Electromagnetic wave scattering from particles of arbitrary
567 shapes," *J. Quant. Spectrosc. Radiat. Transf.* **112**(11), 1636–1645 (2011).
- 568 63. D. Petrov, Y. Shkuratov, and G. Videen, "Light scattering by arbitrary shaped particles with rough
569 surfaces: Sh-matrices approach," *J. Quant. Spectrosc. Radiat. Transf.* **113**(18), 2406–2418 (2012).
- 570 64. A. Macke, J. Mueller, and E. Raschke, "Single Scattering Properties of Atmospheric Ice Crystals," *J.*
571 *Atmospheric Sci.* **53**(19), 2813–2825 (1996).
- 572 65. V. P. Tishkovets, E. V. Petrova, and K. Jockers, "Optical properties of aggregate particles comparable in
573 size to the wavelength," *J. Quant. Spectrosc. Radiat. Transf.* **86**(3), 241–265 (2004).
- 574 66. M. I. Mishchenko and J. M. Dlugach, "Adhesion of mineral and soot aerosols can strongly affect their
575 scattering and absorption properties," *Opt. Lett.* **37**(4), 704–706 (2012).
- 576 67. V. P. Tishkovets and E. V. Petrova, "Spectra of light reflected by aggregate structures of submicron
577 particles," *J. Quant. Spectrosc. Radiat. Transf.* **252**, 107116 (2020).
- 578 68. L. Nagdimunov, L. Kolokolova, and D. Mackowski, "Characterization and remote sensing of biological
579 particles using circular polarization," *J. Quant. Spectrosc. Radiat. Transf.* **131**, 59–65 (2013).
- 580